Breakdown localisation in a pulsed DC electrode system

Iaroslava Profatilova [a],[*], Xavier Stragier [a],[b], Sergio Calatroni [a], Aleh Kandratsyeu [c], Enrique Rodriguez Castro [a], Walter Wuensch [a]

[a] CERN, European Organisation for Nuclear Research, 1211 Geneva, Switzerland
[b] Eindhoven University of Technology, Coherence and Quantum Technology, P.O. Box 513, 5600 MB Eindhoven, The Netherlands
[c] Energy Pulse Systems, Estrada do Paço do Lumiar Polo Tecnológico de Lisboa, Lote 3, 1600-546 Lisboa - Carnide, Lisbon, Portugal

ARTICLE INFO

ABSTRACT

Breakdown localisation is an important diagnostic for studies of vacuum arcs in high electromagnetic field systems such as DC electrodes and radio frequency (RF) accelerating structures. For example, determining the position of individual breakdowns and corresponding distributions of ensembles of breakdowns are important measurements in high-gradient X-band test stands (CERN, SLAC, KEK) where these measurements are made by monitoring the RF signals.

A highly precise breakdown localisation technique has been developed for the CLIC (Compact LInear Collider) pulsed DC electrode systems. These systems are part of the CLIC high-gradient development programme and complementary to RF tests. The optical-based technique discussed here determines where the discharges have occurred by triangulating the emitted light from the breakdown and operates on a breakdown-by-breakdown basis. The implementation of breakdown localisation technique together with a fast Data Acquisition (DAQ) system provides a powerful method of studying breakdown phenomena. The experimental apparatus and its capabilities are presented.

Contents

---

* Corresponding author.
  E-mail address: iaroslava.profatilova@cern.ch (I. Profatilova).

1. Introduction

Vacuum electrical breakdown is an important performance limitation in high-gradient (in the range of 100 MV/m) accelerating structures such as those used in the CLIC study as well as other high-gradient applications such as CompactLight [1–4]. The time required to condition the accelerating structures, that is to bring them up to full operating gradient and pulse length, as well as their ultimate performance, is to a large extent determined by the probability of vacuum RF breakdowns. It is consequently important to find design and fabrication methods to minimise the breakdown probability and improve the performance of the accelerator.

High-gradient studies have been carried out in the context of the development of linear colliders, most extensively in recent years at CERN for the CLIC study. Tests have been made with accelerating structures with different geometries, fabrication techniques and operational algorithms [5–10]. As a complement to these RF tests, pulsed DC systems have been built for dedicated breakdown studies [11–14]. The objective of the systems is to be able to carry out high-gradient and breakdown experiments in conditions similar to the RF tests, for example with pulsed fields, but in a simplified experimental set-up. The pulsed DC systems have a simple planar electrode geometry, which significantly reduces the cost of individual tests compared to RF accelerating structures, and the system can be pulsed with a higher repetition rate, up to 6 kHz for reduced testing time. The shortest pulse length of the pulsed DC system is 500 ns which is in the range of the RF tests, and can be extended to 100 ms. Operational algorithms, which determine how the system recovers from breakdown and how to perform surface conditioning for example, are similar to the RF test stands. Numerous measurements have shown that the overall behaviour of breakdowns in DC and RF systems are similar [13–15] and that many insights obtained in the pulsed DC system can be carried over to the RF tests [16–18].

A vacuum electrical breakdown is characterised by a sudden voltage collapse, with exchange of charge, between two electrodes subject to a high electric field, and is accompanied by large plasma currents, light emitted from atomic excitation. The process leads to surface features and crater creation. In the RF systems, methods have been developed to determine the longitudinal position of the breakdowns along the structure through the relative timing of features, as well as phases, in the incident, transmitted and reflected RF signals. Those techniques have approximately a few mm precision which is sufficient to localise the breakdown with 1–2 cell resolution [19–21]. Until now, it has not been possible to determine the position of the breakdown in the pulsed DC systems at CERN on a breakdown-by-breakdown basis in an analogous way from the current and voltage signals, since breakdowns anywhere on the electrode surfaces affect the signals in the same way. An additional method is thus needed, and a system of cameras that triangulate the light emitted from a breakdown event has been developed for this purpose. The triangulation method in fact results in a far more precise measurement of the breakdown location than in the case of the RF. This system, its capabilities and the initial results are described in this paper.

2. Experimental setup of the pulsed DC system

The first DC pulsed system at CERN has been developed in 2004 [11–13]. Currently the setup consists of three major components: the vacuum chamber, the pulsed High-Voltage (HV) generator, and the Data Acquisition (DAQ) system, which are discussed in detail in the following sections.

2.1. Vacuum chamber

The vacuum chamber of the pulsed DC system contains two round flat electrodes, both with a surface of 40 mm diameter (Fig. 1), therefore called *Large Electrodes System* (LES). The LES has a 14 cm external and a 8.5 cm internal diameter, the latter which limits the size of samples. The electrodes are machined with the same high geometrical accuracy as the CLIC accelerating structures (25 nm roughness), and are separated by a precision-ground ceramic ring, which provides the needed gap between them, typically from 20 to 100 micrometres with a tolerance of a few micrometres. As both electrodes are planar and the gap distance is small compared to the diameter of their surface, they can be considered like a parallel plate capacitor. High voltage with positive polarity is applied to one of the electrodes (the anode), while the second one is grounded (the cathode). The surface electrical field E_{SF} is estimated as:

$$E_{SF} = V/d, \tag{1}$$

where V is the applied voltage and d is gap distance. Since the diameter of the electrodes is much larger than the distance between them, the electric field is uniform on the electrode surface except along the outer edge, where the electric field is enhanced [22–24].

The vacuum chamber is equipped with four viewports of 16 mm diameter with borosilicate glass windows. They give straight line of sight to the electrodes and the gap between them, therefore the light generated during the breakdown can be captured, for example, by cameras placed outside the vacuum chamber directly at the view ports.

A turbo-molecular pumping station is used to achieve a base vacuum level in the range of 10^{-9} mbar. A cold-cathode vacuum gauge records the pressure during the tests in the LES.

2.2. High-voltage generator

A pulsed high-voltage generator is used to apply a voltage to the electrodes, and consequently an electric field in the gap between the electrodes [25]. An Energy Pulse Systems EPULSUS-FPM1-10 unit based on a Marx circuit (simply called Marx generator in the following) generates a high-voltage pulse from a low-voltage DC power supply [26]. The Marx generator designed for the LES can deliver up to 10 kV and 50 A pulses with adjustable square-shaped width in a range from 500 ns to 100 ms. The repetition rate of high-voltage pulses can be controlled and set up to 6 kHz.

2.3. Data acquisition and control system

The HV generator, oscilloscope, vacuum gauge and cameras (see Section 3) have separated control and acquisition software developed in Labview.

For measuring the current during the pulses a current transformer sensor (Bergoz CT-D0.5-B) is used. A HV probe (PMK, PHV-1000) connected to the output of the Marx generator gives information about the voltage, and from this E_{SF} is calculated. The oscilloscope (Lecroy 104 MXi-A) records these voltage and current signals. The schematic in Fig. 2 illustrates how the high-voltage Marx generator is connected to the vacuum chamber and where voltage and current are measured.

Typical current and voltage waveforms for non-breakdown and breakdown cases are shown in Fig. 3. A positive displacement current flows into the electrodes at the beginning of the pulse while charging, and a negative current occurs at the end of the pulse when the electrodes discharge, if no breakdown happens (Fig. 3a). If a breakdown occurs, the current, flowing between the electrodes, increases rapidly to several 10's of Amps (Fig. 3b) and usually it is higher than the charging peak of the displacement current. This current peak is used for breakdown detection. In addition, the voltage across the electrodes drops to almost to zero during breakdown.
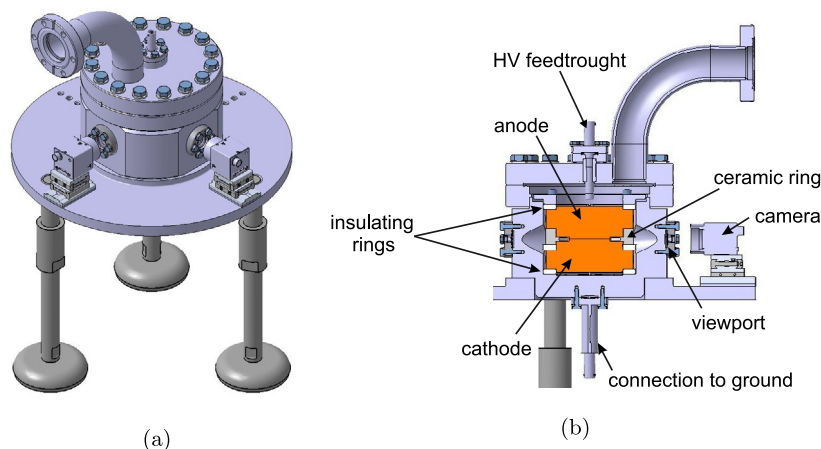
Fig. 1. 3D model of the vacuum chamber for the LES: (a) the view from outside, (b) the cross-section of the chamber.
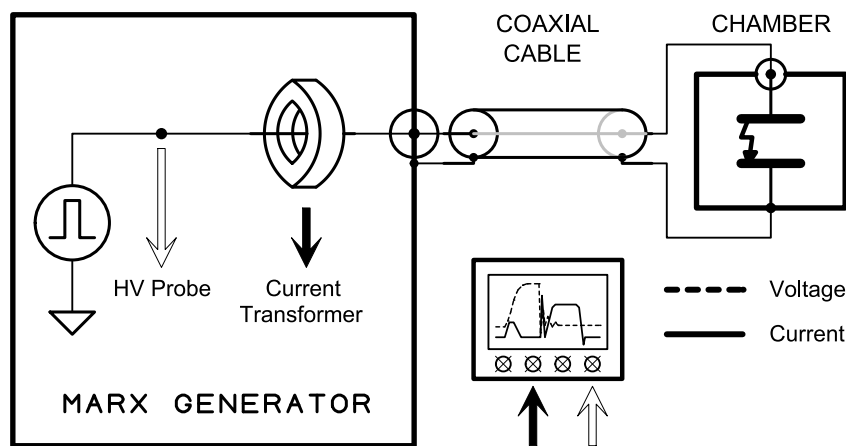

Fig. 2. Schematic of the connections between the Marx generator and the vacuum chamber, with indication of the current and voltage measurement points.

The Marx generator is able to maintain the breakdown current between the electrodes for a certain programmable time, set to 600 ns for these experiments (see Fig. 3b). It mimics the behaviour of the power source in the high power RF tests, which always continues its pulse to the end, even in the case of breakdown.

A Pfeiffer Vacuum Dual Gauge monitors the pressure during the high-voltage pulsing. Typically an increase in pressure up to the 10^{-7} mbar range is observed in correspondence of a breakdown event, thus the vacuum gauge can also be used for breakdown detection.

2.3.1. Operational modes

There are two main operational modes used for testing with the LES, flat and feedback, and these are defined in the Marx generator control software. In the software, parameters that can be set include voltage, pulse width, and repetition rate.

During *flat mode*, HV pulses with fixed amplitude are applied from the HV generator. The voltage is usually chosen to have a breakdown rate (BDR) in the range $10^{-5} - 10^{-8}$ breakdowns per pulse. The BDR is calculated using an exponentially weighted moving average over a 1 million pulses. After a breakdown, pulsing is stopped for 10 s and restarts from 1/5 of the breakdown voltage, and increases every 100 pulses according to a negative exponential function, until the initial fixed voltage is reached or a breakdown occurs. On average, around 20 steps are require for the voltage to reach the set value. This part of the algorithm (so-called *recovering after breakdown*) was implemented to reduce the effect of surface damage in the case of subsequent breakdowns [27,28].

The *feedback mode* is similar to the algorithm currently used in the X-band test facilities at CERN [21,29] for conditioning experiments. The voltage is controlled in an analogous way in the case of the pulsed DC electrode system, as the input power is controlled in the RF case [17, 30]. Pulsing is started with a chosen voltage and continues until either a breakdown happens or a certain number of pulses (n_{max}) have been applied for this iteration. If no breakdown happens, the voltage is increased by an amount dV ($dV = 10$ V for 60 µm gap case) for the next iteration of pulses. If a breakdown happens, the voltage is reduced to 1/5 of the breakdown voltage (V_{BD}) and then increases asymptotically. The voltage reached after breakdown is chosen depending on whether the breakdown is before or after n_{min} number of pulses. If after (i.e. $n > n_{min}$) the voltage increases to V_{BD}, else if it is less (i.e. $n < n_{min}$) than the voltage is calculated as $V_{BD} - (1 - n/n_{min})dV$. There is also a limit for the maximum breakdown rate given as BDR_{max}, this is usually set to 1×10^{-5} breakdowns per pulse. The voltage cannot increase if $BDR > BDR_{max}$. During conditioning experiments, the following parameters were used: $n_{min} = 20\,000$, $n_{max} = 100\,000$, $dV = 0.17$ MV/m $\times$ d, where d is the gap distance between the electrodes (see Eq. (1)).

All results presented in this paper were taken with 1 µs pulse width and 2 kHz repetition rate.

3. Breakdown localisation technique

The localisation technique is based on detecting light emitted during breakdowns with two orthogonal cameras attached to the viewports of the LES (Fig. 1) and triangulating to determine where and when each
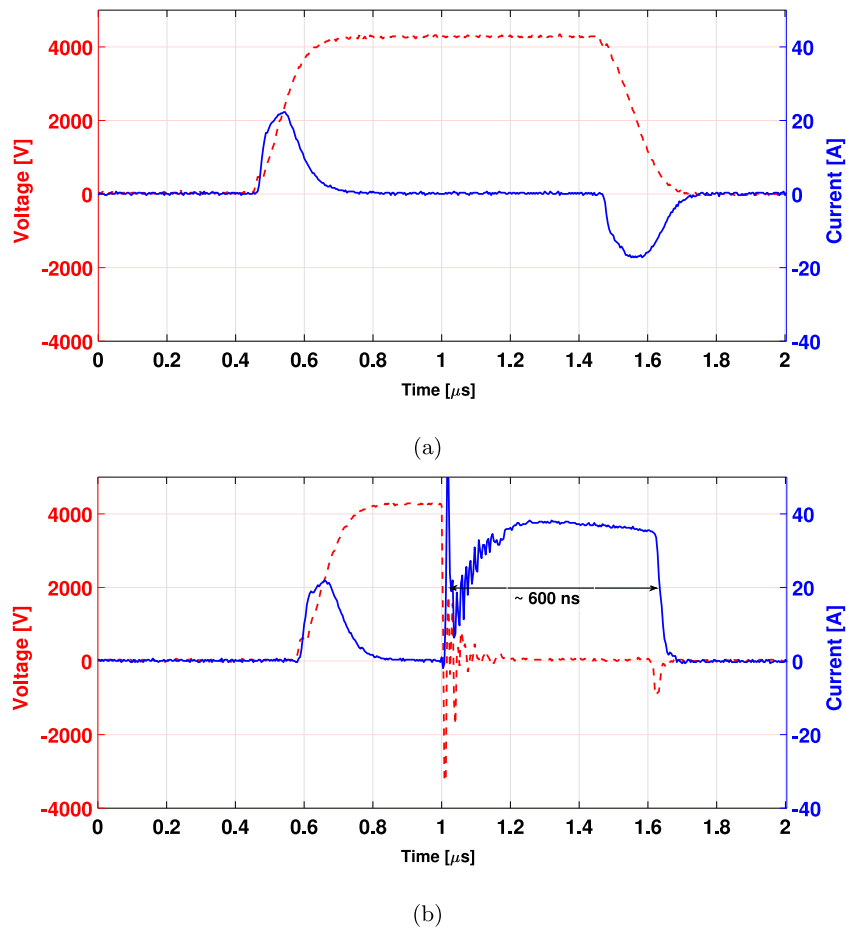
(a)

(b)

Fig. 3. Current and voltage signal from the oscilloscope: (a) non-breakdown high-voltage pulse, (b) breakdown pulse. The blue (solid) line is the current signal. The red (dashed) line is the voltage signal.

breakdown occurred on a pulse-by-pulse basis. The exact sequencing of breakdown locations allows any specific features of breakdown craters to be addressed and correlated during *post-mortem* microscopic analysis. The cameras are also useful for determining if some breakdowns produce light but are not identified by an electrical signal, and *vice versa*. This capability is particularly important when correlated with *post-mortem* microscopic images of the surfaces.

The light emitted during breakdown is monitored through two *camera obscura* attached to two view ports at an angle of 90° (Fig. 4). A vertical slit perpendicular to the electrode surface is located directly behind each viewport. The light generated by the breakdown can be considered as a point source of light in relation to the distance and to the size of the slit. The high accuracy machined electrodes also act as parallel optical mirror with a surface flatness below 1 μm. Therefore the spot of light detected on the CCD camera array, generated by a breakdown, will be in a straight line with the slit and the breakdown position. This type of optical scheme avoids problems with the depth of field and with different type of optical aberrations that are typical for cameras with lenses.

To minimise the line width imaged on the CCD cameras coming from the light of the breakdown, a slit width of 100 μm was found to be the optimum trade-off compatible with sufficient light intensity. The CCD camera array has a horizontal size W = 11.3 mm and consists of 1920 pixels, which means that the actual image position of the breakdown at the CCD is determined by the expression:

$$g_1 = (p_1 - 960.5) \cdot s$$
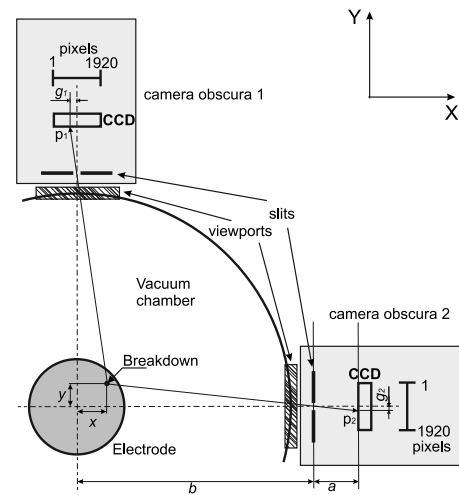$$g_2 = (960.5 - p_2) \cdot s$$

(2)

Fig. 4. Schematic of LES geometry with cameras. The objects are not shown to scale for clarity.

where p_1 and p_2 are the pixel index number of the maximum illumination of the breakdown on respectively camera 1 and camera 2, s being the size of 1 pixel of the camera (i.e. $s = W/1920 \approx 5.9$ μm).

From simple geometric ratios we have:

$$\frac{-g_1}{a} = \frac{x}{b - y}$$
$$\frac{-g_2}{a} = \frac{y}{b - x} \tag{3}$$

where a is the distance from the slit to the CCD array (23.1 mm) and b is the distance from the cathode to the slit (89.6 mm).

To get the coordinates of the breakdown position:

$$x = \frac{-(a + g_2) \cdot g_1 \cdot b}{a^2 - g_1 \cdot g_2}$$
$$y = \frac{-(a + g_1) \cdot g_2 \cdot b}{a^2 - g_1 \cdot g_2} \tag{4}$$

Since the pixels of the CCD cameras have a finite size, breakdowns from nearby points on the electrodes can be detected by the same pixel. This means that such detection has a spatial accuracy limited by the dimension of one pixel. This theoretical limit depends also on the distance of the breakdown to the camera and is about 9 μm on the closer edge of the electrode and about 14 μm on the farthest edge of the electrode for both axes.

The cameras are controlled asynchronously with the Marx generator by repeating the following three steps in a loop:

Step 1: the shutter of the camera is opened.

Step 2: for 3 s the cameras work in accumulation mode.

Step 3: the shutter is closed and the data is read from the sensors of the camera's array and transferred to the computer.

Taking into account the background illumination of the cameras, the software analyses the data and determines whether a breakdown occurred between the electrodes during step 2. If there was a breakdown, the positions p_1 and p_2 of the maximum illumination of the cameras are determined and the x and y positions of the breakdown is calculated by Eq. (4). Also the integral intensity of the discharge arc image is recorded for each camera. In addition a grey scale image file is saved for each detected breakdown.

Step 3 lasts about 10 ms at which time the shutters are closed. This means a duty cycle of 99.7% and thus 0.3% of data (either breakdown or non-breakdown images) are lost by each camera systematically. Data recording could be improved by synchronous triggering of the Marx generator and the cameras.

There are three primary scenarios for images on the cameras following breakdown detection:

1. Each camera registered one light line – **Regular breakdown detection** – in this case the x and y positions are known and the position at the electrode's surface can be calculated.

2. Light is detected only by one camera – **Single camera detection** – in this case only the line/vector where breakdown occurred can be determined. Possible reasons for the lack of an image on the second camera are typically a too low light intensity (for example a breakdown at low voltages), position of the breakdown at the edge of the electrodes far from the camera, not exactly simultaneously opening and/or closing of the shutters, or a combination of these reasons.

3. At least one camera detects more than one line of light – **Multiple breakdown images** – several breakdowns happened during the accumulation mode (step 2). This could be due either to real simultaneous breakdowns in several different places between the electrodes, or to breakdowns occurring on different high voltage pulses during a period less than 3 s and recorded by cameras as one image. Exact position of breakdown cannot be calculated. In this case it is not possible to unambiguously assign positions.

It is sometimes possible to complement the camera images with *post-mortem* microscopic analysis and resolve ambiguities in scenarios 2 and 3.

Table 1
Failure mode analysis.

Generator detection	Oscilloscope detection	Pressure change	Cameras detection	Information
Yes	Yes	No	No	Breakdown in high-voltage cable
Yes	Yes	Yes	No	Breakdown out of surface/gap or breakdown occurred with low voltage for long period, short circuit event
Yes	No	No	No	Non-breakdown pulse detected as breakdown, wrong calibration of the Marx generator
1 pulse	1 pulse	Yes	Multiple breakdown image	Problem with the Marx generator controller

4. Results

4.1. Cross-check of breakdown detection methods

The breakdown localisation technique complements the existing methods of breakdown detection such as the rise of the current during breakdown, used by both the Marx generator and the oscilloscope. This also helps to cross-check the reliability of each data source. Also the rise in pressure monitored by the vacuum gauge controller is used for this reliability check. Based on the experience taken during several months of use of the cameras, information about possible failure modes of the LES was collected and is shown in Table 1. In all cases, breakdown detection by the cameras using the emitted light is the most reliable method. For finding the source of a failure, information from the other three detection methods should be taken to account.

4.2. Numeric accuracy of breakdown detection by cameras

The correlation between the different methods of breakdown detection (using the Marx generator, the oscilloscope and the cameras) has been estimated using data from experiments with several gaps between the electrodes and is presented in Table 2. Breakdown detection using pressure spikes is not presented in this section because of the lack of enough data, as the vacuum gauge was added to the DAQ system only at a later stage. A breakdown is added to the *Total number* column if it is detected at least by one method.

The data from the Marx generator, the oscilloscope and the cameras are associated using time stamps from the recorded data files, that are saved separately for each source. If the time stamps from different sources of a candidate breakdown are within a range of 3 s, it is counted as the same event. A pause of 10 s for the HV pulsing after breakdown (as detected by the Marx generator), implemented for reducing of the background noise in the breakdown localisation system, helps separating the events during data analysis. If one of the method fails to detect the event, it will still be counted, but the full data will not be available. For instance, if a breakdown is not registered by the oscilloscope, the traces of voltage will not be recorded.

The cameras show a good breakdown detection (more than 86% of events recorded by at least one camera). The percentage of regular breakdown detection (see Section 3) is lower with the smaller gap, thus during the test with the 20 μm gap the XY positions of only 43% of the breakdowns were found, while overall detecting 86% of the events. A too low intensity on the CCD leads to these missed breakdowns and it is probably due to poor light propagation in the smaller gap. In all other experiments with a larger gap the XY coordinates could be determined for more than 90% of events, with a breakdown detection in excess of ~ 96% of the total events.

Table 2
Comparison of the number of breakdowns detected by the different sources.

Gap, μm	Total number	Generator	Oscilloscope	Cameras regular detection	Cameras multiple images	Single camera detection	Cameras total
100	7 096	7054 **(99.41%)**	6745 **(95.05%)**	6902 **(97.27%)**	138 **(1.94%)**	11 **(0.16%)**	7051 **(99.37%)**
60	13 060	12 308 **(94.24%)**	12 818 **(98.15%)**	11 907 **(91.17%)**	625 **(4.79%)**	315 **(2.41%)**	12 847 **(98.37%)**
40	1 179	1144 **(97.03%)**	1116 **(94.66%)**	1102 **(93.47%)**	15 **(1.27%)**	23 **(1.95%)**	1140 **(96.69%)**
20	1 430	1416 **(99.02%)**	1035 **(72.38%)**	624 **(43.63%)**	8 **(0.56%)**	607 **(42.45%)**	1239 **(86.64%)**

All three methods show a good agreement. Even though the Marx generator and the oscilloscope use the same principle of detecting breakdowns (current rise between the electrodes), the number of events recorded by each of them is different. The Marx generator fails when the breakdown occurs at the end of a pulse and the electronics no longer has time to react. Detection errors by the oscilloscope most often happen due to loss of communication with the computer.

4.3. Spatial accuracy of breakdown localisation technique

Before and after high-voltage testing the electrodes are examined under a Zeiss Axio Imager optical microscope. The image before the tests gives information on any specific features or defects on the electrodes surface that might locally induce breakdowns. A *post-mortem* microscopic image of the full surface is used to measure the spatial breakdown distribution on the surface, in order to overlay it with the data taken from the cameras. The XY array of the breakdown positions taken with the cameras are hereinafter named *localisation map*.

To perform such an overlay the following affine transformations must be applied to the coordinates of all breakdowns on the localisation map:

- Reflection with $I_0 = -1$ for the bottom electrode, or identity $I_0 = 1$ for the top electrode;
- Rotation by the angle A_0;
- Scaling with the factor R_0;
- Translation along the X and Y axes, with factors T_x and T_y respectively.

Since it is not possible to accurately and unambiguously adjust the relative position of anode and cathode in the chamber, the transformation factors (I_0, A_0, R_0, T_x, T_y) must be calculated after each experiment. It also important to know the transformation factors between the breakdown localisation map and the image of the pristine electrodes, in order to be able to trace the possible effect of any surface features on the breakdowns initiation.

To calculate the transformation factors, we can select some reference breakdowns on the localisation map and overlay them on the corresponding reference craters in the microscopic image using the algorithm from Appendix.

A number of error sources must be considered, the main one being that the microscopic image consists of a matrix of stitched individual images of different parts of the electrodes. Such a composite image contains distortions. Another important source of error comes from the geometrical positioning of the cameras, in particular the uncertainty on the distances a and b (see Fig. 4) for both cameras. Therefore, the overlay using the factors obtained by the method described in Appendix may have a different accuracy in different parts of the electrode image. To have better results, 15–30 reference craters located across the entire electrode surface could be used for overlaying.

We demonstrate the method described above for a data set from a test with a given electrodes pair, and calculate the spatial accuracy for about 600 craters distributed evenly on the electrodes surface. Applying the algorithm using 16 reference craters for calculating the transformation factors, the accuracy of the breakdown localisation technique was estimated by analysing the difference of the breakdown coordinates on the localisation map and the craters on the microscopic image. The result of overlapping the breakdown localisation map and *post-mortem* microscopic image is shown in Fig. 5.

The mean deviation between the XY positioning from cameras and the centre of the corresponding crater on the microscopic images is ±17 μm, less than the observed typical diameter of the breakdown craters (65–230 μm).

5. Application

The camera-based localisation technique combined with the microscopic images can be used to address many important questions related to breakdown. It is possible to unambiguously determine when during operation a breakdown occurred, addressing for example the question of the effect of surface features on breakdowns occurring during conditioning compared to flat mode running. The camera system also gives the sequence of breakdown positions, allowing comparison with RF structures, which show evidence of a statistical pattern of breakdowns occurring in the same location as a previous breakdown distinct from the pattern of those which occur in new locations [9,19,20]. The use of the camera system to address questions such as how a breakdown can become a nucleation site for subsequent breakdowns, how the breakdowns are distributed over the surface and how this distribution evolves with time are elaborated in the following. These important questions are not definitively answered in this article, the objective is limited to showing how the system can be used to address them. The full potential of the system will emerge with further use.

5.1. Breakdowns clustering

The spatial distribution of the breakdowns can give insight into the state of the electrodes surfaces during the experiment. A so-called *hot cell* is sometimes observed in RF tests. These are localised areas with concentrated breakdown activity and can lead to a self-amplifying surface degradation. The camera-based breakdown localisation technique can be used to determine during operation if and where similar *hot spots* form (Figs. 6a and 6b). One probable explanation for this phenomenon is that features of the breakdown spots act as locations of enhanced field emission preferentially nucleating breakdowns on subsequent pulses (see next section).

5.2. Spatial and temporal correlation between breakdowns

The relative tendency for breakdowns to occur in the same location, as opposed to a new location, was investigated using data from experiment done in the flat mode. The spatial distribution data for consecutive breakdowns is shown in Fig. 7. Fig. 7a shows the distribution for the full diameter of the surface, while Fig. 7b is a magnification of the previous histogram in the interval where breakdowns happen no further than 1 mm apart from the previous. There is a maximum close to 100 μm distance. During *post-mortem* analysis it was found that the common size of craters that appear after a breakdown is in the range of 65–230 μm, the maximum on the histogram could then be explained by the preferential creation of breakdown sites at the craters rim [13,16,27,28]. An example of a breakdown crater occurred in the pulsed DC system is shown in Fig. 8 at different magnifications. The microscopic image with high magnification (Fig. 8b) allows to see two breakdown centres.
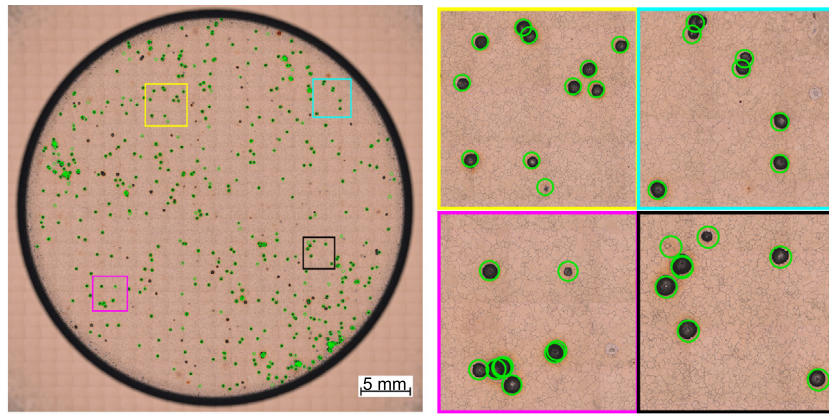
Fig. 5. Comparison of a localisation map and an image from *post-mortem* observation with optical microscope, using 16 reference craters for overlapping. The four images on the right correspond to the four coloured square areas on the left image. The dark spots shown in the optical image are the features left on the surface after breakdowns. The green circles are the positions from the cameras (the circles size is about 150 μm).
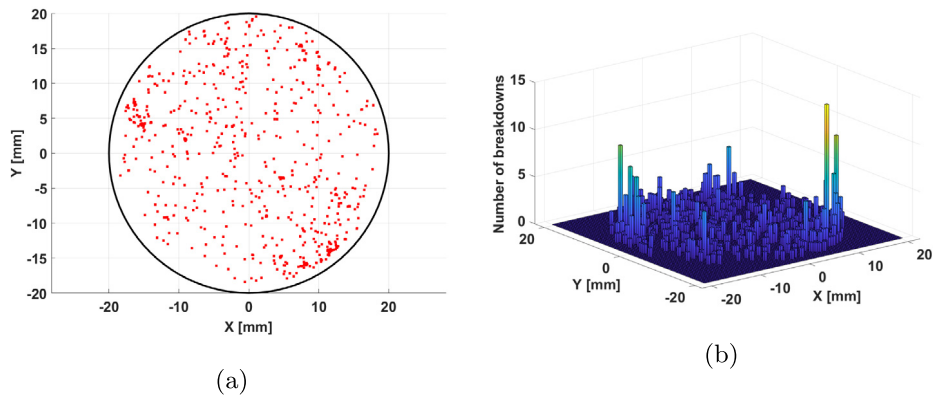

Fig. 6. Breakdown distribution on the surface: (a) 2D mapping, (b) 3D histogram.
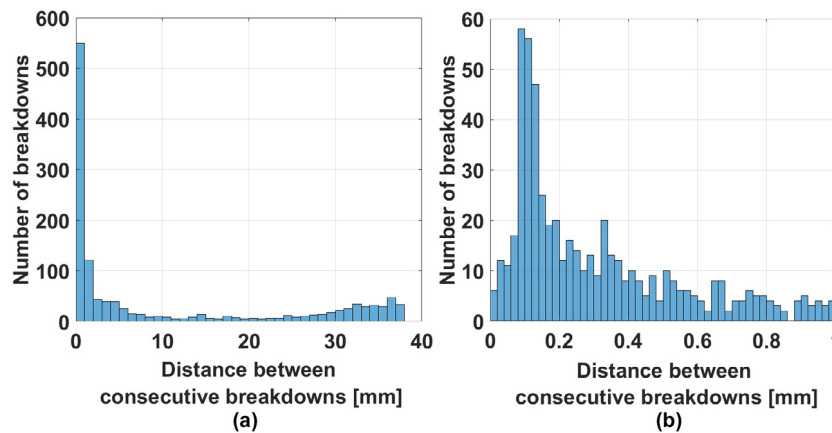

Fig. 7. Distance between consecutive breakdowns: (a) for the complete area, (b) zoomed for the range from 0 to 1 mm.

5.3. Evolution of breakdown distribution

The cameras also give the evolution of preferential locations of the breakdown during the test. Fig. 9 shows the change in the spatial distribution of the first 4000 breakdowns. The data are split into four parts, of 1000 breakdowns each. Initially (1–2000) breakdowns are spread on the total surface (Fig. 9a–c). The next breakdowns (2001–4000) occur mostly on the edge of electrodes (Fig. 9a–c). The initial distribution is more uniform possibly because early conditioning is

"cleaning" extrinsic features which are spread evenly across the electrode surface. Once these features have been conditioned away, the breakdowns concentrate in an area of enhanced electric field at the electrode edge [22–24]. The observation has led to further optimisation of the electrode edge geometry, which will be discussed in future publications. Fig. 9d shows that the histogram shapes evolve from almost flat to the shape already presented and explained in Section 5.2.
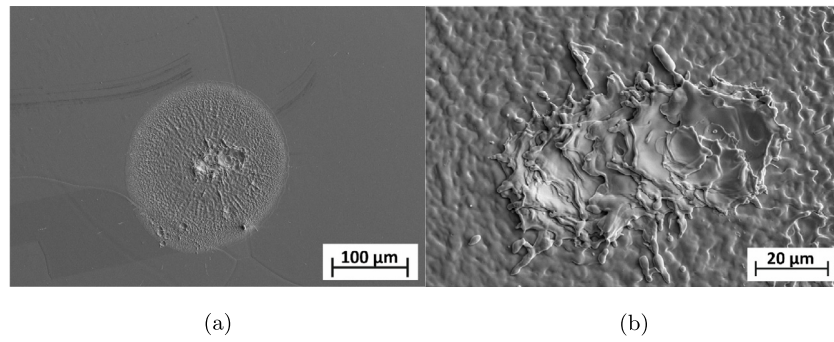
Fig. 8. Scanning Electron Microscope (SEM) images of two overlapping breakdown craters occurred in the pulsed DC system between copper electrodes: (a) 200× magnification, (b) 1000× magnification.
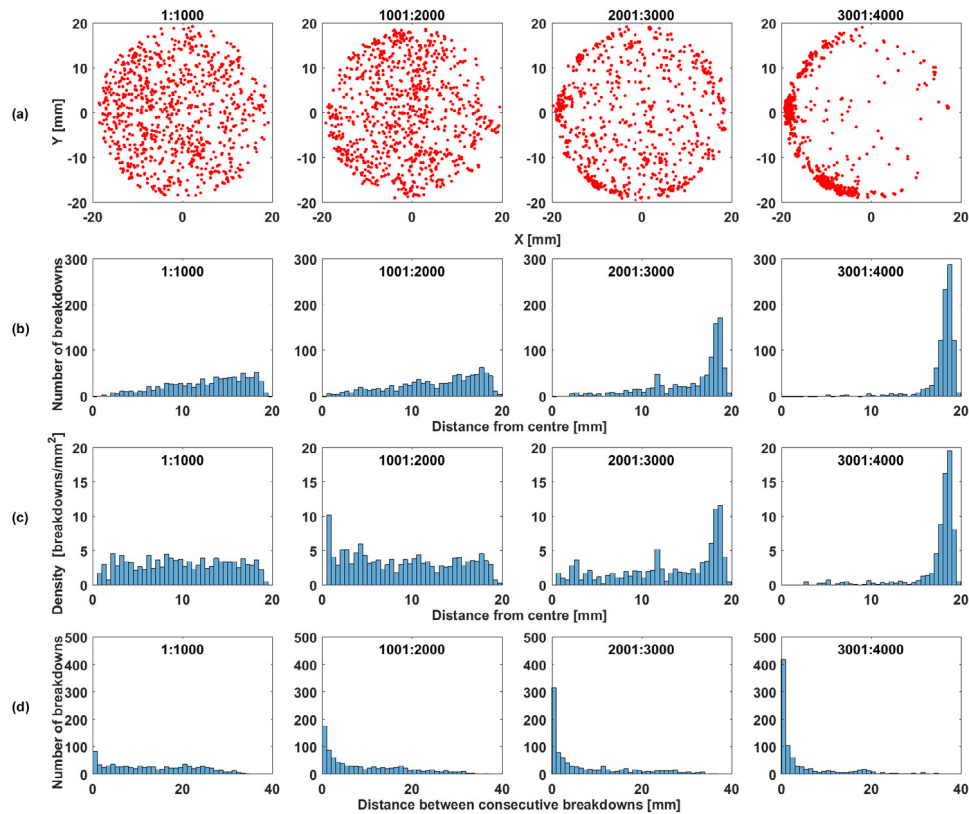

Fig. 9. Evolution of the breakdowns from 1 to 4000 breakdowns: (a) 2D mapping, (b) number of breakdowns vs. distance from the centre, (c) breakdown density vs. distance from the centre, (d) number of breakdowns vs. distance between consecutive breakdowns.

6. Conclusions

A method for detecting and localising breakdowns on a breakdown-by-breakdown basis using triangulation of the emitted light in a pulsed DC system has been developed. Such breakdown localisation technique gives a good agreement (over 90%) with breakdown detection by the Marx generator and the oscilloscope. The spatial accuracy (±17 µm) of the method allows to localise the crater position for most breakdown events and to determine the conditions of the event, such as voltage, distance from previous breakdown, number of pulses after previous breakdown, etc.

These technique and analysis tools will now be used to extend the knowledge about the electrical breakdown phenomena, the effect of material properties on the breakdown initiation (for instance, the effect of the copper grain size on the distance between breakdowns), and the effect of surface electric field on the size of the breakdown crater. Additional information from the cameras will help to connect previous results [5,16] from statistical studies of breakdowns distribution. The preliminary study presented in this paper already shows a good correlation between so-called *primary* and *follow-up* breakdowns, and the distances between them.

Declaration of competing interest

The authors declare that they have no known competing financial interests or personal relationships that could have appeared to influence the work reported in this paper.

Acknowledgements

Appendix. Transformation factors calculation

1. For bottom electrode $I_0 = -1$, for top electrode $I_0 = 1$.
2. N (≥ 3) crater spots (reference craters) are selected on the microscope image of the electrode and their coordinates $C_i = (X_i, Y_i)$ are recorded. Clear, stand-alone craters should be chosen.
3. Breakdowns corresponding to the reference craters are identified on the localisation map. The coordinates on the localisation map of the selected breakdowns set the array $b_i = (x_i, y_i)$
4. From the array of reference craters we compile pairs of craters that form the vectors $[C_i C_j]$. On the localisation map they correspond to vectors $[b_i b_j]$. For a small number of reference craters, it makes sense to choose all possible pairs-vectors, for a large number only the longest vectors are sufficient.
5. The factor R_0 is obtained as the average ratio of lengths $[C_i C_j]$ to lengths $[b_i b_j]$.
6. For each of the vectors $[C_i C_j]$ and $[b_i b_j]$, we determine their angle to the abscissa axis. For all pairs we calculate the difference of these angles. The factor A_0 is obtained as the average of these differences.
7. Apply transformations to (x_i, y_i) with the obtained values of I_0, R_0, A_0. The factors T_x, T_y are the average difference between the coordinates of the obtained results and (X_i, Y_i).
8. For any breakdown detected by the cameras with (x_i, y_i) coordinates the corresponding crater spot on the microscopic image with coordinates (X_i, Y_i) is found as:

$$\begin{pmatrix} X_i \\ Y_i \end{pmatrix} = \begin{pmatrix} I_0 & 0 \\ 0 & 1 \end{pmatrix} \cdot \begin{pmatrix} \cos A_0 & -\sin A_0 \\ \sin A_0 & \cos A_0 \end{pmatrix} \cdot \begin{pmatrix} R_0 & 0 \\ 0 & R_0 \end{pmatrix} \cdot \begin{pmatrix} x_i \\ y_i \end{pmatrix} + \begin{pmatrix} T_x \\ T_y \end{pmatrix}$$
(A.1)

References

[1] M. Aicheler, P. Burrows, M. Draper, T. Garvey, P. Lebrun, K. Peach, N. Phinney, H. Schmickler, D. Schulte, N. Toge, A Multi TeV Linear Collider based on CLIC Technology: CLIC Conceptual Design Report, Tech. rep., 2012, http://dx.doi.org/10.5170/CERN-2012-007.

[2] P. Burrows, N. Catalan-Lasheras, L. Linssen, M. Petric, A. Robson, D. Schulte, E. Sicking, S. Stapnes, The Compact Linear e+ e- Collider (CLIC)-2018 Summary Report, CERN Yellow Reports: Monographs, CERN, 2018.

[3] W. Wuensch, High-gradient RF development and applications, in: Proceeding of LINAC 2016, East Lansing, MI, USA, 2016, pp. 368–373, http://dx.doi.org/10.18429/JACoW-LINAC2016-TU2A04.

[4] A. Latina, M. Aicheler, A. Aksoy, A. Bernhard, J. Clarke, A. Cross, G. D'Auria, R. Dowd, D. Esperante Pereira, W. Fang, A. Faus-Golfe, M. Ferrario, E. Gazis, R. Geometrante, M. Jacewicz, A. Mostacci, F. Nguyen, F. Pérez, J. Priem, T. Schmidt, D. Schulte, S. Stapnes, W. Wuensch, Compactlight design study, in: JACoW Publishing (Ed.), 60th ICFA Advanced Beam Dynamics Workshop on Future Light Sources, 2018, http://dx.doi.org/10.18429/JACoW-FLS2018-WEP1WC02.

[5] C. Adolphsen, W. Baumgartner, K. Jobe, F. Le Pimpec, R. Loewen, D. McCormick, M. Ross, T. Smith, J.W. Wang, T. Higo, Processing studies of X-band accelerator structures at the NLCTA, in: Proceeding of the 2001 Particle Accelerator Conference, no. 1, Chicago, Illinois, 2002, pp. 478–480. http://dx.doi.org/10.1109/pac.2001.987546.

[6] C. Adolphsen, Normal-conducting rf structure test facilities and results, in: Proceeding of the 2003 Particle Accelerator Conference, 2004, pp. 668–672, http://dx.doi.org/10.1109/pac.2003.1289005.

[7] J.W. Wang, J.R. Lewandowski, J.W. Van Pelt, C. Yoneda, G. Riddone, Gudkov Dmitry, T. Higo, T. Takatomi, Fabrication technologies of the high gradient accelerator structures at 100 MV/m range, in: Proceeding of IPAC2010, Kyoto, Japan, 2010, pp. 3819–3821.

[8] L. Laurent, S. Tantawi, V. Dolgashev, C. Nantista, Y. Higashi, M. Aicheler, S. Heikkinen, W. Wuensch, Experimental study of rf pulsed heating, Phys. Rev. Spec. Top.- Accel. Beams 14 (4) (2011) 041001, http://dx.doi.org/10.1103/PhysRevSTAB.14.041001.

[9] F. Wang, Breakdown characteristics study on an 18 cell X-band structure, in: AIP Conference Proceedings, Santa Cruz, California, USA, 2009, p. 373–379. http://dx.doi.org/10.1063/1.3080934.

[10] X. Wu, J. Shi, H. Chen, J. Shao, T. Abe, T. Higo, S. Matsumoto, W. Wuensch, High-gradient breakdown studies of an X-band compact linear collider prototype structure, Phys. Rev. Accel. Beams 20 (5) (2017) 52001, http://dx.doi.org/10.1103/PhysRevAccelBeams.20.052001.

[11] M. Kildemo, New spark-test device for material characterization, Nucl. Instrum. Methods Phys. Res. A 530 (3) (2004) 596–606, http://dx.doi.org/10.1016/j.nima.2004.04.230.

[12] A. Descoeudres, T. Ramsvik, S. Calatroni, M. Taborelli, W. Wuensch, DC breakdown conditioning and breakdown rate of metals and metallic alloys under ultrahigh vacuum, Phys. Rev. Spec. Top.- Accel. Beams 12 (3) (2009) 32001, http://dx.doi.org/10.1103/PhysRevSTAB.12.032001.

[13] J. Kovermann, Comparative studies of high-gradient RF and DC breakdowns (Ph.D. thesis), 2010.

[14] N. Shipman, Experimental study of DC vacuum breakdown and application to high-gradient accelerating structures for CLIC (Ph.D. thesis), 2014.

[15] S.A. Barengolts, V.G. Mesyats, V.I. Oreshkin, E.V. Oreshkin, K.V. Khishchenko, I.V. Uimanov, M.M. Tsventoukh, Mechanism of vacuum breakdown in radio-frequency accelerating structures, Phys. Rev. Accel. Beams (2018) http://dx.doi.org/10.1103/PhysRevAccelBeams.21.061004.

[16] W. Wuensch, A. Degiovanni, S. Calatroni, A. Korsbäck, F. Djurabekova, R. Rajamäki, J.G. Navarro, Statistics of vacuum breakdown in the high-gradient and low-rate regime, Phys. Rev. Accel. Beams 20 (1) (2017) 11007, http://dx.doi.org/10.1103/PhysRevAccelBeams.20.011007.

[17] A. Korsbäck, L.M. Morales, I. Profatilova, E.R. Castro, W. Wuensch, S. Calatroni, T. Ahlgren, Vacuum electrical breakdown conditioning study in a parallel plate electrode pulsed DC system, 2019, arXiv:1905.03996.

[18] A. Degiovanni, W. Wuensch, J.G. Navarro, Comparison of the conditioning of high gradient accelerating structures, Phys. Rev. Accel. Beams (2016) http://dx.doi.org/10.1103/PhysRevAccelBeams.19.032001.

[19] J. Nelson, M. Ross, J. Frisch, F. Le Pimpec, D. McCormick, Use of acoustic emission to diagnose breakdown in accelerator rf structures, in: Proceeding of the 2003 Particle Accelerator Conference, Portland, Oregon, USA, 2003, pp. 1279–1281.

[20] R. Rajamäki, Vacuum arc Localization in CLIC Prototype Radio Frequency Accelerating Structures (M.Sc. thesis), Helsinki University, 2016.

[21] B. Woolley, High Power X-band RF Test Stand Development and High Power Testing of the CLIC Crab Cavity (Ph.D. thesis), 2015.

[22] J.R. Nagel, Solving the generalized Poisson equation using the finite-difference method, IEEE Antennas Propag. Soc. Feature Artic. (2012) 1–18.

[23] G.W. Parker, Electric field outside a parallel plate capacitor, Amer. J. Phys. 70 (5) (2002) 502–507, http://dx.doi.org/10.1119/1.1463738.

[24] S. Catalán Izquierdo, J.M. Bueno Barrachina, C.S. Cañas Peñuelas, F. Cavallé Sesé, Capacitance evaluation on parallel-plate capacitors by means of finite element analysis, Renew. Energy Power Q. J. 1 (07) (2017) 613–616, http://dx.doi.org/10.24084/repqj07.451.

[25] I. Profatilova, High field studies for CLIC accelerating structures development, in: CERN Proceedings, Vol.1/2017, 2017, pp. 127–133, http://dx.doi.org/10.23727/CERN-Proceedings-2017-001.127.

[26] L.M. Redondo, A. Kandratsyeu, M.J. Barnes, S. Calatroni, W. Wuensch, Solid-state marx generator for the compact linear collider breakdown studies, in: 2016 IEEE International Power Modulator and High Voltage Conference, IPMHVC 2016, 2017, http://dx.doi.org/10.1109/IPMHVC.2016.8012824.

[27] G.A. Mesyats, Explosive processes on the cathode in a vacuum discharge, IEEE Trans. Electr. Insul. EI-18 (3) (1983) 218–225.

[28] J.W. Wang, G.A. Loew, Field Emission and RF Breakdown in High-Gradient Room-Temperature Linac Structures, Tech. Rep., 1997.

[29] A. Degiovanni, S. Doebert, W. Farabolini, A. Grudiev, J. Kovermann, E. Montessinos, I. Syratchev, R. Wegner, W. Wuensch, A. Solodko, B. Woolley, High-Gradient test results from a CLIC prototype accelerating structure: TD26CC, in: Proceeding of IPAC2014, Dresden, Germany, 2014, pp. 2285–2287, http://dx.doi.org/10.18429/JACoW-IPAC2014-WEPME015.

[30] N. Catalan-Lasheras, A. Degiovanni, S. Doebert, W. Farabolini, J. Kovermann, G. McMonagle, S. Rey, I. Syratchev, L. Timeo, W. Wuensch, B. Woolley, J. Tagg, Experience operating an X-band high-power test stand at CERN, in: Proceeding of IPAC2014, Dresden, Germany, 2014, pp. 2288–2290, http://dx.doi.org/10.18429/JACoW-IPAC2014-WEPME016.